Research Article | Vol. 25, No. 18 | 4 Sep 2017 | OPTICS EXPRESS 21851

Optics EXPRESS

Towards a holographic approach to spherical aberration correction in scanning transmission electron microscopy

VINCENZO GRILLO,[1] AMIR H. TAVABI,[2] EMRAH YUCELEN,[3] PENG-HAN LU,[2] FEDERICO VENTURI,[1,4] HUGO LAROCQUE,[5] LEI JIN,[2] ALEKSEI SAVENKO,[3] GIAN CARLO GAZZADI,[1] ROBERTO BALBONI,[6] STEFANO FRABBONI,[1,4] PETER TIEMEIJER,[3] RAFAL E. DUNIN-BORKOWSKI,[2] AND EBRAHIM KARIMI[5,7,*]

[1]*CNR-Istituto Nanoscienze, Centro S3, Via G Campi 213/a, I-41125 Modena, Italy*
[2]*Ernst Ruska-Centre for Microscopy and Spectroscopy with Electrons, Forschungszentrum Jülich, 52425 Jülich, Germany*
[3]*Thermo Fisher Scientific, PO Box 80066, 5600KA, Eindhoven, The Netherlands*
[4]*Dipartimento FIM Universitá di Modenae Reggio Emilia, Via G Campi 213/a, I-41125 Modena, Italy*
[5]*Department of Physics, University of Ottawa, 25 Templeton St., Ottawa, Ontario, K1N 6N5 Canada*
[6]*CNR-IMM Bologna, Via P. Gobetti 101, 40129 Bologna, Italy*
[7]*Department of Physics, Institute for Advanced Studies in Basic Sciences, 45137-66731 Zanjan, Iran*
[*]*ekarimi@uottawa.ca*

Abstract: Recent progress in phase modulation using nanofabricated electron holograms has demonstrated how the phase of an electron beam can be controlled. In this paper, we apply this concept to the correction of spherical aberration in a scanning transmission electron microscope and demonstrate an improvement in spatial resolution. Such a holographic approach to spherical aberration correction is advantageous for its simplicity and cost-effectiveness.

OCIS codes: (090.1000) Aberration compensation; (090.1995) Digital holography; (120.3180) Interferometry.

References and links

1. M. Haider, S. Uhlemann, E. Schwan, H. Rose, B. Kabius, and K. Urban, "Electron microscopy image enhanced," Nature **392**(6678), 768 (1998).
2. O. Krivanek, N. Dellby, and A. Lupini, "Towards sub-Å electron beams," Ultramicroscopy **78**(1), 1–11 (1999).
3. P. Hawkes, "Aberration correction past and present," Phil. Trans. R. Soc. A **367**(1903), 3637–3664 (2009).
4. O. Scherzer, "Über einige fehler von elektronenlinsen," Zeitschrift für Physik A Hadrons and Nuclei **101**(9), 593–603 (1936).
5. L. Allen, R. Angel, J. D. Mangus, G. A. Rodney, R. R. Shannon, and C. P. Spoelhof, "The Hubble space telescope optical systems failure report," NASA Report (1990).
6. M. Uchida and A. Tonomura, "Generation of electron beams carrying orbital angular momentum," Nature **464**(7289), 737–739 (2010).
7. B. J. McMorran, A. Agrawal, I. M. Anderson, A. A. Herzing, H. J. Lezec, J. J. McClelland, and J. Unguris, "Electron vortex beams with high quanta of orbital angular momentum," Science **331**(6014), 192–195 (2011).
8. V. Grillo, G. Carlo Gazzadi, E. Karimi, E. Mafakheri, R. W. Boyd, and S. Frabboni, "Highly efficient electron vortex beams generated by nanofabricated phase holograms," Appl. Phys. Lett. **104**(4), 043109 (2014).
9. J. Verbeeck, H. Tian, and P. Schattschneider, "Production and application of electron vortex beams," Nature **467**(7313), 301–304 (2010).
10. R. Shiloh, Y. Lereah, Y. Lilach, and A. Arie, "Sculpturing the electron wave function using nanoscale phase masks," Ultramicroscopy **144**, 26–31 (2014).
11. N. Voloch-Bloch, Y. Lereah, Y. Lilach, A. Gover, and A. Arie, "Generation of electron Airy beams," Nature **494**(7437), 331–335 (2013).
12. V. Grillo, E. Karimi, G. C. Gazzadi, S. Frabboni, M. R. Dennis, and R. W. Boyd, "Generation of nondiffracting electron Bessel beams," Phys. Rev. X **4**(1), 011013 (2014).

#295959 https://doi.org/10.1364/OE.25.021851
Journal © 2017 Received 15 May 2017; revised 11 Aug 2017; accepted 11 Aug 2017; published 30 Aug 2017

Optics EXPRESS

13. V. Grillo, A. H. Tavabi, F. Venturi, H. Larocque, R. Balboni, G. C. Gazzadi, S. Frabboni, P.-H. Lu, E. Mafakheri, F. Bouchard, R. E. Dunin-Borkowski, R. W. Boyd, M. P. J. Lavery, M. J. Padgett, and E. Karimi , "Measuring the orbital angular momentum spectrum of an electron beam," Nat. Commun. **8**, 15536 (2017).
14. M. Linck, B. McMorran, J. Pierce, and P. Ercius, "Aberration-corrected stem by means of diffraction gratings," Microscopy and Microanalysis **20**(S3), 946–947 (2014).
15. V. Grillo, J. S. Pierce, E. Karimi, T. R. Harvey, R. Balboni, G. C. Gazzadi, E. Mafakheri, F. Venturi, B. J. McMorran, S. Frabboni, and R. W. Boyd, "Structured electron beam illumination: a new control over the electron probe weird probes and new experiments," Microscopy and Microanalysis **21**(S3), 25–26 (2015).
16. V. Grillo, E. Karimi, R. Balboni, G. C. Gazzadi, S. Frabboni, E. Mafakheri, and R. W. Boyd, "Toward holographic approach to spherical aberration correction in stem," IMC conference **IT-1-P-6140** (2014).
17. R. Shiloh, R. Remez, and A. Arie, "Prospects for electron beam aberration correction using sculpted phase masks," Ultramicroscopy **163**, 69–74 (2016).
18. O. L. Krivanek, J. Rusz, J.-C. Idrobo, T. J. Lovejoy, and N. Dellby, "Toward single mode, atomic size electron vortex beams," Microscopy and Microanalysis **20**(03), 832–836 (2014).
19. D. Pohl, S. Schneider, P. Zeiger, J. Rusz, P. Tiemeijer, S. Lazar, K. Nielsch, and B. Rellinghaus, "Atom size electron vortex beams with selectable orbital angular momentum," Sci. Rep. **7**, 934 (2017).
20. E. J. Kirkland, *Advanced Computing in Electron Microscopy* (Springer Science & Business Media, 2010).
21. C. Boothroyd, A. Kovács, and K. Tillmann, "Fei titan g2 60-300 holo," JLSRF **2**, 44 (2016).
22. V. Grillo and F. Rossi, "Stem_cell: A software tool for electron microscopy. part 2 analysis of crystalline materials," Ultramicroscopy **125**, 112–129 (2013).
23. E. Mafakheri, A. Tavabi, P.-H. Lu, R. Balboni, F. Venturi, C. Menozzi, G. Gazzadi, S. Frabboni, A. Sit, R. Dunin-Borkowski, E. Karimi, and V. Grillo, "Realization of electron vortices with large orbital angular momentum using miniature holograms fabricated by electron beam lithography," Appl. Phys. Lett. **110**(9), 093113 (2017).
24. J. Silcox, P. Xu, and R. F. Loane, "Resolution limits in annular dark field stem," Ultramicroscopy **47**(1-3), 173–186 (1992).
25. P. Nellist and S. Pennycook, "Subangstrom resolution by underfocused incoherent transmission electron microscopy," Phys. Rev. Lett. **81**(19), 4156 (1998).
26. V. Grillo and E. Carlino, "A novel method for focus assessment in atomic resolution STEM HAADF experiments," Ultramicroscopy **106**(7), 603–613 (2006).
27. V. Grillo and E. Rotunno, "Stem_cell: A software tool for electron microscopy. part I simulations," Ultramicroscopy **125**, 97–111 (2013).
28. J.M. Cowley, "Coherent interference in convergent-beam electron diffraction and shadow imaging," Ultramicroscopy **4**, 435–449 (1979).
29. J.E. Barth and P. Kruit, "Addition of different contributions to the charged particle probe size," Optik **101**, 101–109 (1996).

1. Introduction

The successful correction of spherical aberration in the late 1990s solved a long-standing limitation in transmission electron microscopy (TEM) [1–3]. This limitation, which has always afflicted the field even after Scherzer discovered that the use of cylindrically symmetrical electrostatic and magnetic lenses leads to strictly positive spherical aberration [4], results from the impossibility of generating arbitrary fields in vacuum. Spherical aberration must be compensated by an opposite aberration, which is usually produced by a set of electric and magnetic multipoles, whose complexity rivals that of the adaptive optics of the Hubble telescope [5]. The primary complication of this approach is associated with the use of strong magnetic fields in coupled multipoles that must be highly stable and perfectly matched. As a consequence, there is still a need to develop alternative aberration correction concepts.

Recent progress in nanofabrication, in combination with inspiration drawn from methods in light optics, is resulting in the development of new innovative phase elements for electron microscopy [6–8]. Unprecedented control over the phase of an electron beam can now be achieved by using nanofabricated electron holograms, which consist of electron-transparent materials that are patterned to have controlled thickness modulations. Amplitude holograms can also be used to introduce phase variations in an electron beam by means of an initial amplitude modulation [9], although they are not as efficient as phase elements. Phase holograms, which are also known as kinoforms, can be classified into two categories. First, there are diffractive (or "off-axis") holograms [7, 8], which consist of diffraction gratings and control the phase of

Optics EXPRESS

an electron beam through modulations in the spacing of the grating. Second, there are in-line holograms [6,10], in which the phase that is imparted to the electron beam is directly proportional to the thickness profile of the material. Such devices were first used for the generation of electron vortex beams and subsequently in further applications that demonstrated their flexibility [11–13]. The ability to arbitrarily modulate the phase profile of an electron beam has led several groups to independently propose holographic methods for the correction of spherical aberration. For example, Linck *et al.* [14] and Grillo *et al.* [15, 16] proposed a diffractive approach, but did not show how to remove the spurious diffracted beams that appear in the specimen plane of the microscope. Some of the co-authors of this paper initially used a blazed hologram [8, 16] to transfer most of the intensity of the electron beam to a single spot. Shiloh *et al.* [17] proposed using an in-line hologram for the correction of the main aberrations of an electron probe. Such an in-line approach has several advantages over its diffractive counterpart, in part due to the fact that the ray path is aligned with the propagation axis of the electron beam. However, it is challenging to implement in practice because the thickness of the slab must be controlled with nanometer precision over a large transverse area. In addition, regions where the phase wraps over 2π radians must also be accounted for by a sudden change in thickness. A failure to introduce the correct abrupt phase jump results in additional unwanted intensity components in the probe, even in cases where the overall phase correction is accurate. It is inevitable that part of the electrons in the beam experience some energy losses upon propagating through the holographic aperture. In methods relying on an in-line hologram, these inelastically scattered electrons are no longer properly focused in the probe due to chromatic aberration, and they can result in a blurred background in the STEM image. Furthermore, they can lead to ghost signals in EELS (Electron Energy Loss Spectroscopy). An advantage of diffractive off-axis holograms is that they strongly suppress the background attributed to inelastically scattered electrons. In particular, inelastic scattering is mostly absent in the diffracted beams because the grid spacing of the hologram is greater than the typical coherence length of inelastically scattered electrons. Second, most inelastically scattered electrons coming from the zeroth diffraction order do not go through our small aperture that selects the first diffraction order. This filtering occurs because the area of this aperture is about two orders of magnitude smaller than that of the diffuse cone of inelastically scattered electrons.

Here, we demonstrate that a combination of an off-axis diffractive hologram and modified electron illumination optics can be used to produce an aberration corrected probe in a scanning TEM (STEM). The key point of our work is that the new configuration, when optimized, will allow control over spherical aberration in a single isolated diffraction spot, opening the way to holographic control over aberrations.

2. Materials and methods

Figure 1 shows a schematic diagram of our setup, in which we use a nanofabricated hologram to generate a single spherical aberration corrected beam. The configuration is based on the typical illumination system of an FEI Titan TEM, with the convergence and defocus of the electron beam controlled independently by the coupled excitation of the two condenser lenses C2 and C3. The remaining lenses, including the objective lens and the condenser mini-lens Cm, are usually fixed. In the present configuration, we placed a nanofabricated hologram in the C2 condenser aperture plane. We then changed the excitation of the C3 lens, so that an intermediate image of the field emission gun (FEG) (*i.e.*, the cross-over) was at the C3 aperture plane, while Cm was adjusted so that the probe was focused on the specimen. The convergence semi-angle could be adjusted by changing the C2 lens and refocusing with the C3 lens. This modification was achieved by over-riding the standard working conditions of the microscope, which normally only allow for coupled action of the C2 and C3 condenser lenses over a limited range. In order to find the position of the crossover after the C2 lens, we searched for a configuration for which the

Optics EXPRESS

excitation of C3 did not affect the beam. We found that a small defocus of C2 could be used to localize this crossover in the C3 aperture plane. We were then able to select a single chosen beam

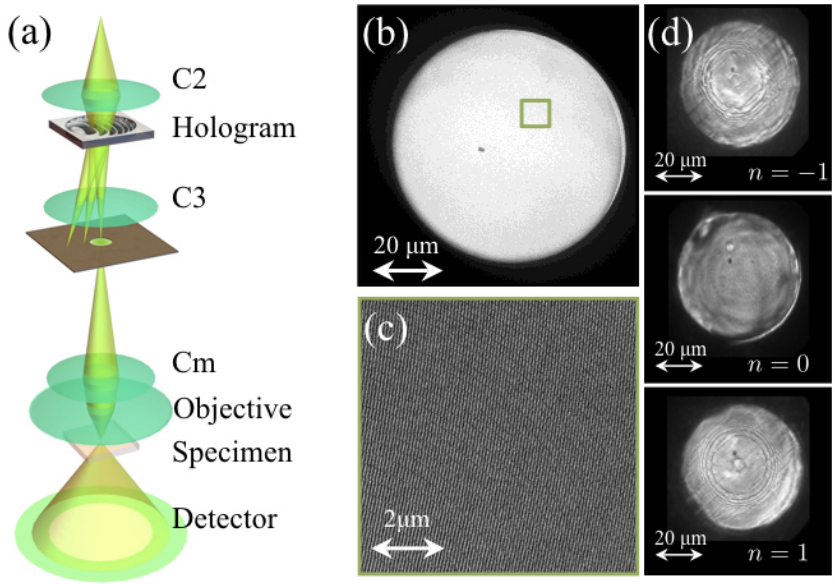

Fig. 1. a) Electron microscope configuration used to isolate a single holographically-corrected electron beam. b) Scanning electron micrograph of a hologram that was placed in the C2 aperture plane. c) Magnified image of b). d) Images obtained and formed by selecting a single diffraction order from the grating. These images are analogous to "dark field" and "bright field" images obtained in diffraction contrast TEM. As further elaborated in the Appendix, the visible rings are points of phase discontinuity that arise from the hologram's piecewise phase correction.

that had been diffracted by the C2 hologram. The separation between the diffraction orders was on the order of 2 μm and our selection was performed with a specially fabricated C3 aperture that was slowly and cautiously aligned with the beam. This aperture eliminated much of the diffuse and inelastic scattering in our apparatus. Particular care was taken with the beam alignment to ensure that it was "coma-free" before reaching the aperture. A similar approach was recently proposed for the isolation of vortex beams [18, 19].

In order to design a hologram that can correct for spherical aberration, we recall that the phase that is imparted by an electromagnetic lens onto a generic wavefront can be formulated in Fourier space as [20]

$$\begin{aligned}\chi &= -\pi\Delta f\lambda k^2 + \pi 2\lambda^3 C_s k^4 + \pi \mathrm{A}_2\lambda k^2\cos\left(2(\theta-\theta_{2A})\right)\\ &\quad +2\pi 3\lambda^2\mathrm{A}_3 k^3\cos\left(3(\theta-\theta_{3A})\right) + 2\pi 3\lambda^2\mathrm{B}_2 k^3\cos\left(\theta-\theta_B\right)+\ldots\ ,\end{aligned} \tag{1}$$

where λ is the wavelength of the electron beam, k is its radial wave vector, θ is the transformed azimuthal coordinate and the other terms describe different aberrations. The first two terms in Eq. (1) represent the well-known rotationally symmetric aberrations defocus Δf and spherical aberration C_s. The remaining terms correspond to axial coma (parameterized by B_2 and θ_B), two-fold astigmatism (parameterized by A_2 and θ_{2A}) and three-fold astigmatism (parameterized by A_3 and θ_{3A}), while higher-order aberrations are neglected here. In a STEM that has no multipolar C_s corrector, an appropriate use of probe tilt and quadrupole stigmators allows coma

Optics EXPRESS

and A_2 to be compensated. Therefore, when C_s is corrected completely, A_3 becomes the first resolution-limiting aberration. In order to achieve this situation, we aim to impart a phase with a negative value of C_s to the electron beam, while using the defocus Δf as an optimization parameter. We therefore work with a nanofabricated hologram, whose thickness is determined by the phase given by the expression

$$\varphi(\rho, \phi) = \varphi_0 F\left[Q\rho\sin(\phi) - \frac{2\pi}{\lambda}\left(\frac{1}{4}C_s\rho^4 - \frac{1}{2}\Delta f\rho^2\right)\right], \tag{2}$$

where ρ and ϕ are polar coordinates in the plane of the hologram and the $Q\rho\sin(\phi)$ term enables the use of a probe tilt, which is necessary to produce the main grating frequency. We employ a coordinate system where ρ is in angle units and can be expressed in terms of the x, y Cartesian coordinates with the relation $\rho = \sqrt{x^2 + y^2}/(40\ \mu\text{m})12$ mrad. Q is specifically the carrier frequency whose value, in our coordinates, is given by $2\pi(1024/12)$ mrad. φ_0 is the modulation depth parameter of the hologram and $F(x)$ is a function that describes the groove profile of the hologram that is required for it to impart a phase of x to the beam. This parameter was modified in our experiment in order to improve the efficiency of the device. The polar coordinates are calibrated in angle according to the measured convergence of the beam. We aimed for a convergence semi-angle of 12 mrad and assumed a C_s value of 2.7 mm and a wavelength λ of 1.97 pm, which are consistent with the standard conditions of the microscope that was used for the experiment (an FEI TITAN G2 60-300 [21], operated at 300 keV and equipped with a C-twin objective lens). The choice of 12 mrad is close to the maximum value that is allowed in the presence of three-fold astigmatism (whose A_3 parameter is typically close to 1 μm) and other aberrations. Although we deliberately worked with $\Delta f \neq 0$ holograms in some tests, the primary experiments were performed with holograms for which $\Delta f = 0$. A $\Delta f \neq 0$ parameter can be used to extend the region over which the imparted phase varies slowly, which can facilitate fabrication of the hologram. The hologram produces many diffraction orders, which are associated with different phase modulations. In particular, the 0^{th} diffraction order experiences no phase modulation, while the n^{th} diffraction order acquires an "artificial" spherical aberration phase of $\varphi = -n2\pi\lambda\left(14C_s\rho^4\right)$. Only the 1^{st} diffraction order ($n = 1$) acquires a phase profile that exactly compensates for the spherical aberration of the microscope, which, in this case, comprises 10-15% of the beam's total transmitted intensity [23]. Clearly, this correction can be obtained for only a fixed voltage and beam convergence. However, for real applications, a set of multiple holograms can be prepared for different experimental conditions on a single sample. In fact, up to 9 holograms can be fit on a single 3 mm disk. Several additional experimental factors can make the implementation of such a phase profile more difficult. Since we are using a relatively large aperture, the compensation should be as precise as possible, resulting in the need for very precise hologram fabrication. In addition to this requirement, it is necessary to spatially separate each diffraction order from every other one.

The holograms that we used in our experiments were designed using the software STEM CELL [22] and fabricated using electron beam lithography (EBL), according to a similar protocol to that introduced in our previous work [23]. We covered a circular area with a diameter of 80 μm surrounded by a 50 nm-thick SiN membrane covered with a 200 nm-thick Au layer to produce an effective diaphragm. The resulting membrane is described in Fig. 1(b),(c). The hologram has 4k × 4k pixels and a rectangular groove profile. This approach results in a piecewise correction of the phase, which becomes smoother at larger radial distances and could be improved in the future by using a focused ion beam (FIB) fabrication process to provide a sinusoidal groove profile.

Just as for in-line nanofabricated holograms, piecewise defined correction can cause spurious intensity components in the probe (*i.e.*, delocalization). Here, we concentrate primarily on the intensity of the contrast transfer function (CTF) in the frequency domain, which should not be

Optics EXPRESS

affected significantly by this problem. The CTF can be calculated from the transverse phase distribution of the beam in the aperture (*i.e.*, $A(k) = \exp(i(\chi + \varphi))$ for k within the aperture and 0 elsewhere) by using the autocorrelation (here indicated by $\otimes$) [24, 25]

$$\mathrm{CTF}(k) = A(k)^* \otimes A(k), \tag{3}$$

which is not affected by phase discontinuities. However, sudden phase jumps may create local intensity modulations in the function $A(k)$. These modulations are visible when the aperture is imaged in "dark field" conditions and only one of the beams diffracted by the hologram is selected by the C3 aperture (see Fig. 1(d)). They were also used as markers to achieve better alignment of the hologram on the beam's propagation axis.

3. Results and discussion

In order to demonstrate the imaging properties of our setup, we used a test material consisting of a FIB-prepared lamella of Si oriented along [110]. Figure 2(a) shows an atomic-resolution STEM

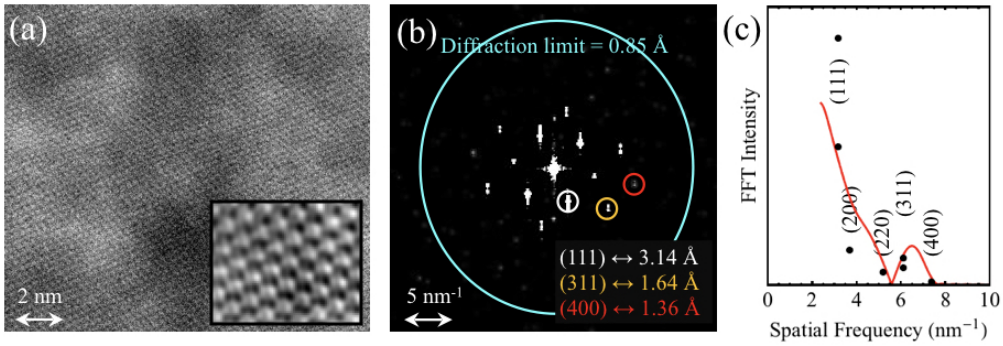

Fig. 2. a) Raw STEM image recoded using a single spot $n = 1$ (main image) and a filtered image of the lattice (inset). b) Fourier transform of the experimental STEM image, showing a faint but visible spot corresponding to the (4,0,0) periodicity in Si. c) Intensities of the peaks in the Fourier transform plotted as a function of spatial frequency. An example of a simulated CTF with a "similar" trend is also shown. We did not try to fit the (2,0,0) intensity, as it should be almost completely inhibited.

annular dark-field (ADF) image recorded using a single diffraction probe, which was scanned across the sample following phase modulation by the hologram. For our STEM experiments, the detection semi-angle of the annular detector was set to 24-145 mrad. The inset shows a higher magnification STEM image, displayed following the use of a filtering procedure that is described elsewhere [21]. In the Fourier transform of the STEM image, which is shown in Fig. 2(b), periodicities as small as 1.36 Å , which correspond to the Si (4,0,0) spacing, are present. The visibility of these fringes, which cannot be detected under standard working conditions for which the Scherzer resolution is approximately 1.9Å, can be considered as a first benchmark. For comparison, we provide a STEM-HAADF (high-angle annular dark-field) image obtained in standard Scherzer working conditions in Fig. 3. Its diffraction pattern only shows orders going up to the (111), (200) and (022) periodicities. Notice how the signal-to-noise ratio in Fig. 3 is better than in Fig. 2. This difference arises from the fact that the STEM probe diffracted by the hologram is dimmer than it usually is under standard microscope configurations. To overcome this limitation, the diffraction efficiency of our corrector hologram needs to be increased. Nonetheless, in spite of the probe's lower intensity, Fig. 2 still displays more details than Fig. 3.

Optics EXPRESS

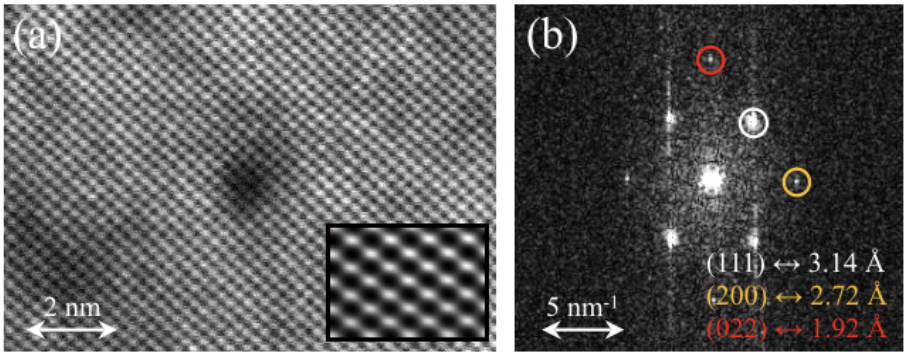

Fig. 3. a) Raw STEM image recorded under Scherzer working conditions and a filtered image of the lattice (inset). b) Fourier transform of the experimental STEM image, only showing higher order periodicities corresponding to (111), (200), and (022). Note that the 200 reflection is a forbidden reflection, that is, it can only be excited through multiple scattering.

Figure 2(c) shows the effective intensity of these frequency components, plotted alongside a simulated CTF that was obtained by assuming the formation of a linear image $I(k) = \mathrm{CTF}(k)O(k)$ and a simplified object function

$$O(k) = \sum_i \delta(k - k_i) \exp\left(-\frac{k^2}{\sigma^2}\right) \tag{4}$$

with $\sigma = 9$ nm^{-1}. A more detailed description of the function $O(k)$ is discussed in [26] and references therein. Although a full dynamical simulation would be more representative of the data in Fig. 2(c), it is difficult to perform such a calculation without having further physical details about the probe. Nevertheless, it is likely that the CTF that is consistent with the data is characterized by strong intensity up to 4 nm^{-1} and a secondary region that peaks at 7 nm^{-1}. It should be noted that the CTF that is shown in Fig. 2(c) corresponds to a case where spherical aberration is not completely compensated. This imperfect compensation could have different origins. Given that we used our condenser system in a rather unconventional fashion, our initial hypothesis was that the large aberrations of the condenser could cause a residual effect on the probe. Such effects would not be corrected. However, as there is a large angular magnification generated by the objective, the maximum angle subtended by the condenser aperture is much smaller than (approximately 0.03 times) that subtended by all of the electron beams. Since the aberration phase is defined by the term $C_s k^4$, even an aberration as large as 1 m cannot have a significant influence on the quality of the beam.

Conversely, we estimated that we had an error of up to 3% in our angle calibration. Though consistent with the tolerances of our diffraction calibration, these errors arise from standard defects in the definition of the hologram's borders and from deformations in the diffraction images. This seemingly small uncertainty can have a large effect on the shape of the final wavefront. Again, the quartic k-dependence of the aberrated phase results in the fact that the hologram produces a compensating ptase that is approximately 12% smaller or larger than that expected. We estimated that the latter effect corresponds to a maximum residual aberration of ±0.3 mm. Considering all of these factors, the CTF shown in Fig. 2 was chosen to correspond to residual aberrations of $C_s = 0.3$ mm and $\Delta f = 60$ nm. Based on these values and on the methods provided in [29], we can provide a detailed prediction of how these remaining aberrations affect our beam. More specifically, our experimental parameters, which consist of an effective

Optics EXPRESS

brightness of $B = 1.5 \times 10^7$ A m^{-2} sr^{-1} V^{-1}, a chromatic aberration of $C_c = 2.7$ mm, an energy spread $dE = 0.7$ eV, and a probe current $I_{\text{probe}} = 5$ pA, effectively produce a limit of 0.14 nm that is in agreement with our experimental results.

Other effects may be associated with residual charging of the hologram [22]. Nevertheless, as further discussed in the Appendix, our data show that the hologram produces a nearly stationary phase distribution up to 8-9 mrad from its center, confirming that the electron-optical configuration performs correctly up to at least this angle. In order to achieve definitive control over C_s in the future, it will be necessary to account for such additional aberrations using an approach that involves better alignment and calibration of the apparatus. All of these factors can be taken care of in future experiments, allowing for near-perfect aberration correction.

Our results are already significant, given the resolution that is demonstrated. They are not, however, intended to compete with multipolar correction. Instead, they are intended to provide a low cost solution for aberration correction, as well as for the two corrector principles to work together, for example by allowing a lower current to be used in the multipolar lenses of a corrector to provide improved stability of its electronics. This possibility will be a driving force towards improving the present stability of electron-hologram-based correctors, in order to overcome that of technologically mature state-of-the-art multipolar correctors. Though we cannot comment on the long-term stability of HSQ-based holograms fabricated using EBL, we can report that FIB-based fabrication schemes for SiN holograms produce very durable devices. In particular, such holograms can be used for many experiments, amounting to a duration of at least 50 hours of work over a period of two years, without undergoing any forms of visible damage.

4. Conclusion

We have demonstrated an electron-optical configuration for the holographic correction of spherical aberration in a STEM probe. Our setup is based on a nanofabricated off-axis hologram, which introduces a spherical aberration that is opposite to the nominal aberration. We have achieved single beam scanning of a Si [110] sample with a transfer function that extends up to 0.136 nm. Residual aberrations are attributed to additional aberrations introduced by imprecise calibration of the convergence angle of the microscope and to possible charging of the hologram membrane.

Appendix

I. Characterization of the probe's corrected profile

Here, we explain the presence of the black circles in the images in Fig. 1(d) based on the features of our hologram. These black circles primarily arise from the fact that EBL holograms are characterized by discrete jump in the hologram lines and that the image formed by its first diffraction order results from the beam's amplitude and phase in the pre-specimen focal plane. Therefore, the discrete jumps in the hologram lines, which translate to sudden changes in phase, will manifest themselves as zeros in the beam's intensity. In Fig. 4, we display simulated data attributed to this effect by showing how it arises for a discrete step hologram.

The effect of these phase discontinuities in the probe can also be analyzed from an approach based on Appendix B of [27]. By using the stationary phase argument, the distance from the probe centre where the intensity is non-zero can be calculated. In practice, if there is a single k coordinate in the probe such that $\Delta\mathbf{r} = \frac{\nabla_k(\chi(k)+\varphi(k))}{2\pi}$ then the point at $\Delta\mathbf{r}$ is characterized by some intensity. Therefore, a phase discontinuity in the probe forming at the aperture plane produces scattered or spurious intensity components at consistent distances from the probe centre. Nevertheless, as reported in the main text, the integrated contribution of these components is not sufficient to change the CTF. The same argument holds for phase discontinuities in in-line holograms. In the following, we provide further discussions surrounding the parametrization of the CTF that we employed in the main text. Given an aperture function $A = \exp(i\chi(k))$ for

Optics EXPRESS

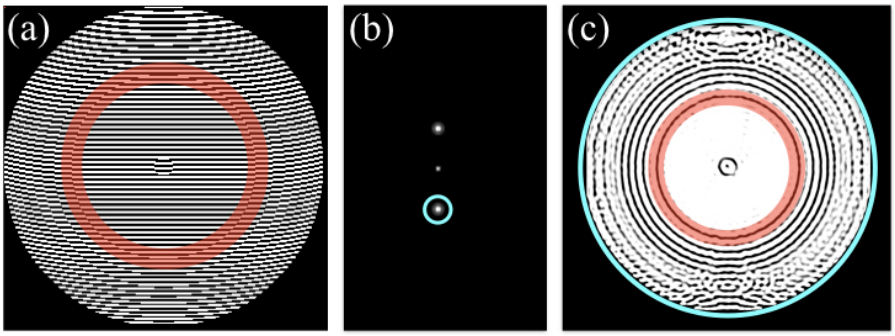

Fig. 4. Simulated output obtained from an effective discrete step hologram. (a) Discrete step hologram used in the simulations. The first discrete jump in the pattern of the hologram is highlighted in red. (b) Diffraction pattern obtained from the hologram. The first diffraction order that is selected by the microscope's aperture is circled in blue. (c) The demodulated image of the aperture plane which is characterized by dark lines corresponding to the discontinuities of the hologram. A dark ring in the profile of the beam resulting from the discrete phase jumps of the hologram is highlighted in red.

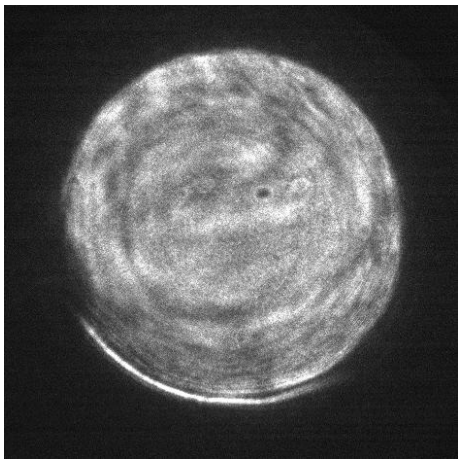

Fig. 5. Ronchigram of amorphous carbon using the $n = 1$ beam. The beam clearly shows a "circle of infinite magnification" whose presence is caused by a substantial spherical aberration.

$k < k_{\max}$ and 0 elsewhere, all zeros of the CTF are associated to conditions where the phases χ are found to vary within a large range, e.g. within $[0, 2\pi]$. This can be demonstrated using an expression for the CTF taken from [24] $\mathrm{CTF(Q)}=\int |A(k)|\,|A(k+Q)| \cos\left(\chi(k) - \chi(k+Q)\right) dk$ As long as $\chi(k)$ and $\chi(k+Q)$ are within a confined. range (say between 0 and $\pi/2$), then their difference is close to zero and we have an integral in the form of a strictly positive function.

Suppose now that χ is a nearly stationary function up to $k < k_{\mathrm{FLAT}}$ and strongly varying for $k > k_{\mathrm{FLAT}}$. We can assume to first approximation that the integral is determined by k values such that $k < k_{\mathrm{FLAT}}$ and $k + Q < k_{\mathrm{FLAT}}$. For the larger values of k, the integral is zero due to rapid oscillations and the system becomes equivalent to having a pupil extension up to k_{FLAT}. In our case, the extension of the nonzero part of the CTF hints at a $\lambda k_{\mathrm{FLAT}}$ value of about 8-9 mrad.

Optics EXPRESS

II. Residual spherical aberrations

Here, we show a Ronchigram of amorphous carbon, obtained with the $n = 1$ beam, that confirms that a residual spherical aberration is still present. This Ronchigram can be found in Fig. 5. In fact, the presence of the “circle of infinite magnification" [28] indicates that the main aberrations in the probe are still defocus and spherical aberrations. Specialized software and images with a good signal-to-noise ratio would allow these two aberrations to be separately analyzed.

Funding

Alexander von Humboldt Foundation; Canada Research Chairs; European Union’s Seventh Framework Programme (FP7/2007-2013)/ ERC(320832).

Acknowledgments

V. G. is grateful for support from the Alexander von Humboldt Foundation. H. L. and E. K. acknowledge the support of the Canada Research Chairs (CRC). R. D.-B. is grateful to the European Research Council for funding under the European Union’s Seventh Framework Programme.